6. AC ramp breakdown testing and analysis

6.1 Experimental procedure

In Chapter 1, a brief overview was given of the types of physical processes that might determine the electrical breakdown strength of a system. Recalling that the likelihood of some catastrophic instability occurring will be a function of both applied field and time, constant stress tests (with time as the dependent variable) would provide the most statistically complete information. Such tests are very time-consuming, however, and since it is not possible to make time the independent variable, a ramped stress test is in practice the most efficient way to obtain large amounts of data.

An electrical testing procedure based upon the general considerations laid down in ASTM standard D149-87 [6.1],[6.2],[6.3] was used. A circuit diagram is shown in Figure 6.1. The sample for testing was immersed in Dow Corning 200/20 cs silicone fluid, between two 6.3 mm steel ball bearings. A 50 g load was added to the upper electrode (total mass 56 g) in order to eliminate the film of oil between the electrode and the sample which would affect the breakdown data. A 50 Hz voltage was then increased from zero up to a maximum of 18 kV at 50 V s^{-1}, the sample failing at around 10 kV. Hosier [6.4] found that 15 breakdowns were sufficient to cause pitting on the electrodes, reducing the effective breakdown strength. A conservative approach was taken in this study, changing the electrodes after every five breakdowns. The silicone fluid was changed at the start of every day, since it is known that fluid contaminated by electrical activity would eventually lower the measured breakdown strengths.

The principal advantage of this geometry over pin-plane and plane-plane geometries is the small amount of material required for each breakdown. Each sample consisted of a 25 mm diameter disk of material with a thickness of 70±2.5 μm. It might be argued that charge injection processes could limit the number of breakdowns that could be performed on each disk. However, in practice, 5 breakdowns were performed on each disk, and cumulative experience on over 100 disks provided reassurance that this did not introduce

any noticeable problems into the data. Another potential advantage of sampling small areas is that the effect of anomalous defects can be contained within smaller clusters of data, meaning that less data need to be left-censored to obtain datasets which truly represent the background (anomalous defect-free) population. Also, the field divergence with this film thickness closely approximates parallel-plate geometry at the contact tangents.

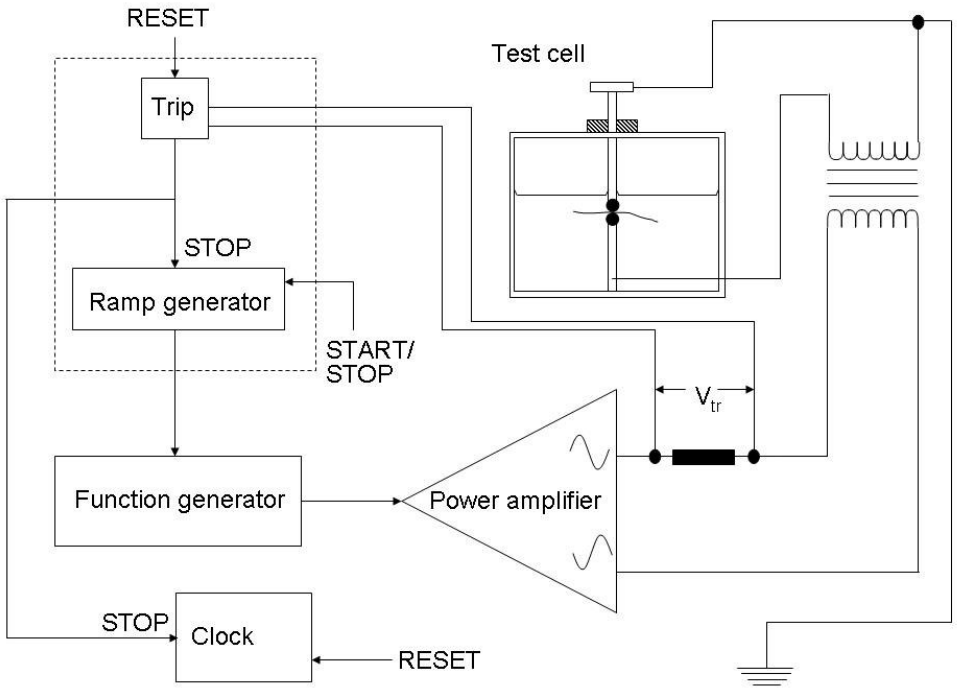

Figure 6.1 Schematic diagram for electrical breakdown rig.

Tests conducted with recessed electrodes or epoxy-encapsulated samples can yield LDPE breakdown strengths around 600 kV mm^{-1} [6.5]; this is over three times as high as the values obtained by Hosier using a ball-bearing setup [6.4]. Furthermore, Martin [6.6] found that the breakdown strengths of XLPE samples varied strongly with the roughness of the sample surface. Clearly then, the breakdown strengths obtained from this technique should not be regarded as indicative of the intrinsic material breakdown strength. Rather, they are a measure of the combined effect of internal processes and external discharges in the oil. These hot electrons will provide an additional source of both charge carriers and kinetic energy for heating and electrical erosion. The

consequence of using a ramped test together with a ball-bearing apparatus is that this is a multi-modal test. The failure mode is a function of the applied voltage and of the electrical environment at the electrode-oil-sample triple point (and of course, the latter is in turn dependent on the former.) Nonetheless, it is considered that the benefit of generating large amounts of data for statistical analysis outweighs the inability of this technique to test specific mechanistic models.

During early experiments, the audible onset voltage for corona voltage between the high tension lead (HTL) and the surrounding air was very low – around 9 kV. Corona discharge would add a high frequency component onto the applied signal, possibly accelerating the breakdown processes. It was found that shielding the HTL with a PTFE pipe and suspending it from the top of the cage with nylon fishing wire increased the audible corona onset to 12 kV, which was above the breakdown strength of most of the samples. The explanation for this is that a counter-field was established to suppress the corona due to charges deposited on the internal wall of the pipe.

The HT voltage was measured using a 10 000:1 potential divider and Precision Gold WG020 digital multimeter (not shown in Figure 7.1 for simplicity.) Initially, it was feared that these devices could be damaged by transients from the breakdowns, and so they were calibrated every week against the laboratory standard voltmeter until confidence in their long-term stability could be established. There was also concern about the possibility of nonlinearity in the transformer (Foster no. ED355;) in practice, it proved possible to draw a chord from the origin to an output voltage – time plot with a gradient accurate to with 5%. The frequency was stable, as observed on an oscilloscope (Hameg HM203-4 20 *MHz*), with a drift of at most 1% over the course of 10 min. It proved necessary incrementally to adjust the ramp rate after each ramp; otherwise, it could drift by up to 6% per hour. The effect of this uncertainty was further minimised by recording the breakdown voltage directly rather than by back-calculation from the breakdown time.

6.2 Statistical background: Selecting the best distribution

There are 3 questions that need to be considered when selecting an appropriate distribution for breakdown statistics:

<1> Is there a suitable model or family of models that might generate a testable distribution?

<2> Does the distribution have sufficient flexibility to conform to the observed data?

<3> Is the distribution easy to handle computationally, both in parameter estimation and confidence bound estimation?

In practice, <3> is generally less important than it was historically. A sophisticated software package (Weibull^{++}7^{TM} from Reliasoft$^{®}$) was used to facilitate the data analysis in this research. Questions <1> and <2> stand in opposition to each other in the sense that the more flexible the distribution is, the less predictive power the physical model can have.

Useful compromises between <1> and <2> can be best obtained by realising that a number of asymptotic distributions exist for large samples of stochastic events drawn from the same population. The best known of these is the central limit theorem, which states that the sampling distribution of the mean of any population approaches a normal distribution with increasing sample size [6.7]. Alternatively, a variable which can be considered as the multiplication, rather than the addition, of the outcomes of a large number of stochastic processes drawn from the same population could be represented by the log-normal distribution. Because of their ease of handling, both the normal and log-normal distributions were used extensively in the early days of life data analysis, but it has not been possible to find families of physical models which could generate breakdown statistics through such addition or multiplication mechanisms [6.8].

More relevant are the asymptotic distributions of extreme values (sampling maxima and minima,) discussed in detail by Lawless [6.9]. Gumbel

[6.8] showed that three asymptotically stable extreme value distributions (AEV) exist, termed the 1st, 2nd and 3rd AEVs. The second is of no importance to electrical engineers (the time domain is negative, and all the samples have failed by t=0!) The first, otherwise known as the Gumbel distribution, has the form:

$$F(x) = 1 - \exp\left(-\exp\left(\frac{x - x_t}{x_c}\right)\right), -\infty < x < +\infty \qquad (6.1)$$

where $F(x)$ is the cumulative probability of failure at time (or in our case, voltage) x, x_t is a threshold time below which no failures will occur and x_c is a scale parameter. The disadvantages of the Gumbel distribution are that they have no shape-modifying parameter and that like the 1st AEV they give a finite probability of failure for negative times. Dissado [6.10], however, insists that the Gumbel distribution is the most appropriate AEV for ramp breakdown initiated by a distribution of field-enhancing defects or partial discharges in voids. The 1st AEV can also be appropriate for liquid dielectric breakdown [6.11].

It is in fact the 3rd AEV that is the most widely used breakdown distribution, due to its flexibility. This was reported by Weibull in 1951 and is the standard distribution recommended by the IEEE [6.12],[6.13].

$$F(x) = 1 - \exp\left(-\left(\frac{x - x_t}{\alpha}\right)\right)^{\beta}, x \geq x_t \qquad (6.2)$$
$$F(x) = 0, x < x_t$$

where α and β are the location and shape parameters of the distribution. Under some conditions, such as where there is a critical threshold for space charge injection, the threshold parameter will take a non-zero value. However, in most cases there is simply not enough evidence to justify the use of a 3-parameter distribution. Cacciari *et al.* [6.14] have analyzed the breakdown data of thin PE films. They note that although, for their data, a goodness of fit test favours a 3-parameter model over a 2-parameter one, this is an artefact of increased mathematical versatility.

Weibull deduced this model, as explained by Ross [6.15], by considering that the cumulative distribution function (cdf) of the mechanical strength of a chain containing *n* links should have the same shape as the strength of any one link. The underlying mechanisms must have fractal characteristics in space or time. The highly idealised thermodynamic fluctuation model [6.1] could produce this, but the real value of a Weibull distribution is actually due in its mathematical flexibility, especially in those cases (which may be the vast majority) where the underlying mechanisms are not fractal.

Plots of the probability density functions (pdfs) and cdfs of Weibull distributions under α=1 and various β are shown in Figures 6.2 and 6.3.

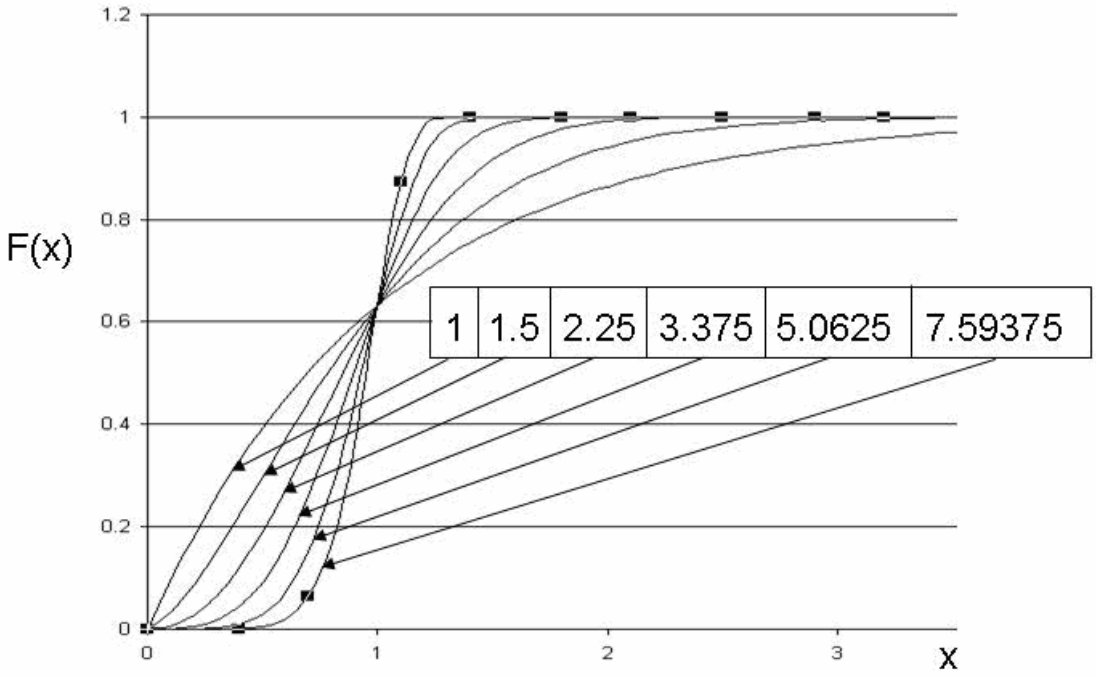

Figure 6.2: CDF of Weibull function under α=1 and various values of β.

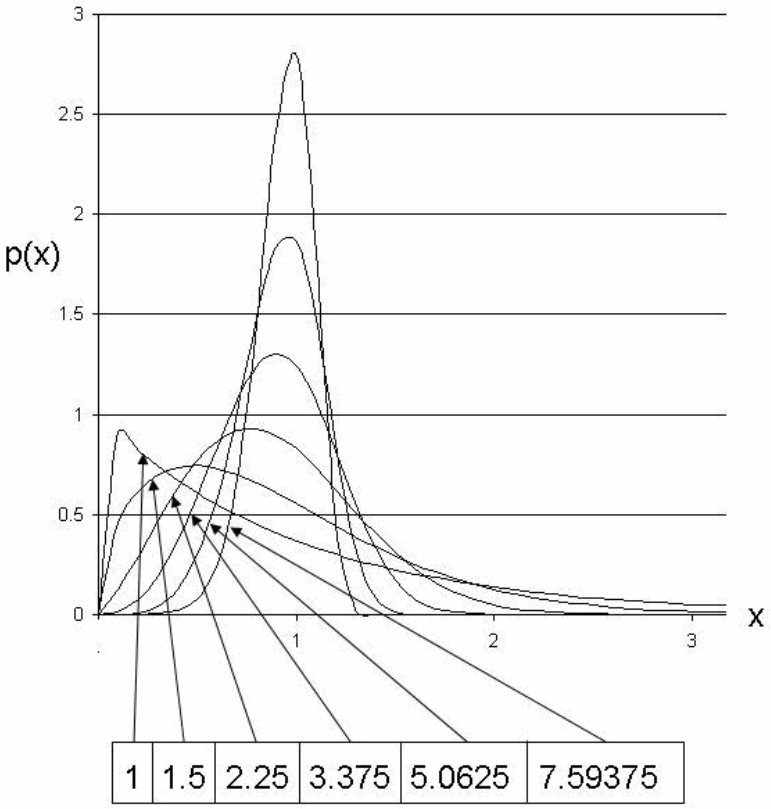

Figure 6.3: PDF of Weibull function under α=1 and various values of β.

Chi-squared goodness of fit tests were conducted on the data prior to Weibull analysis. Overall, it was found that the generalised gamma and 3 parameter Weibull functions gave the best fit, with the data fitting least well to the 1- and 2- parameter exponential distributions*. The first two functions were rejected as they are 3-parameter distributions, so it was decided to conduct a narrower comparison of the normal, Weibull and Gumbel functions. The goodness-of-fit rankings are shown in Table 6.1 below.

*Much interconnectedness can be found between different types of distribution. If event rates follow a normal distribution in time, event quantities will have a Poisson distribution in sampled time intervals and an exponential distribution of times between successive events. If successive events can then be thought of as causing cumulative damage, the time to critical damage will have a Gamma distribution. The exponential distribution is a limiting case of the 1AEV, 3AEV and Gumbel functions; being highly specified, it is relatively inflexible mathematically.

Dataset	Normal	Weibull 2 (3 AEV)	Gumbel (1 AEV)
1	1	1	2
2	3	2	1
3	2	1	1
4	2	1	3
5	1	2	3
6	3	2	1
7	3	2	1
8	3	2	1
9	1	2	3
10	1	2	3
11	3	2	1
12	3	2	1
13	1	2	3
14	1	2	3
15	1	2	3
Mean rank	1.93	1.8	2
Standard deviation in rank	0.96115	0.414039	1

Table 6.1: Chi-squared goodness-of-fit rankings for most of the datasets of between 15 and 25 datapoints obtained in this study. The 2 parameter Weibull consistently provides the best fit.

The 2-parameter Weibull distribution is the best overall fit considered in terms of its mean rank, the standard deviation of its rank position and the fact that it is never the worst distribution – though it is seldom the best.

In order to estimate the Weibull parameters, it is necessary first to rank the breakdowns in order of voltage and then estimate the true probability of failure from each point by median rank estimation. In other words, the cumulative probability of failure for each data point needs to be estimated. The key here is to realise that it is possible to assign a unique cumulative probability of failure $F_i(x)$ for each ranked data point i (out of n) such that the probability that the estimate is too high (or low) will follow a binomial distribution [6.7]. Median rank estimation, therefore, assigns a value of 50% to this probability:

$$0.5 = P\left[F_i(x) = \frac{k}{i} \right] = \left(\frac{i}{k} \right) [F_i(x)]^k [1 - F_i(x)]^{i-k}, k = 0,1,.....,i \qquad (6.3)$$

In order to solve this equation, a transformation must be made to an incomplete beta function. However, it is more convenient to use a simple approximation, several of which are available, such as the Bernard estimator [6.16]:

$$F_i(x) = \frac{i - 0.3}{n + 0.4} \qquad (6.4)$$

A double log plot is then made of equation (6.2) (setting x_t=0), ideally yielding a straight line. Next, the parameters *α* and *ß* need to be estimated. Linear regression will be biased toward the extremes of the distribution, and so it might be argued that Maximum Likelihood Estimation (MLE) gives better estimates of the parameters. This reverses the question "Given this set of parameter values, what is the most probable model output?" to "Given this set of outputs, what are the most likely parameter values?" Firstly, a likelihood function *L(α,β)* is defined, which is the product of the pdfs *f(x:α,β)* for each data point:

$$L(\alpha, \beta) = f(x_1 : \alpha, \beta) \times f(x_2 : \alpha, \beta) \times ..... \times f(x_3 : \alpha, \beta) \qquad (6.5)$$

It is more practical to maximise log(*L(α,ß)*) than L(*α,ß*), and the relevant equations for 2-parameter Weibull are:

$$\frac{1}{\beta_{ML}} = \frac{\sum_{i=1}^{n} (x_i^{\beta_{ML}}) \ln x_i}{\sum_{i=1}^{n} (x_i^{\beta_{ML}})} - \frac{1}{n} \sum_{i=1}^{n} \ln x_i \qquad (7.6)$$

$$\alpha_{ML} = \left[\frac{1}{n} \sum_{i=1}^{n} x_i^{\beta_{ML}} \right]^{\frac{1}{\beta_{ML}}} \qquad (7.7)$$

Equation (6.7) can be solved by Newton-Raphson on an initial guess of β provided by least squares regression. A likelihood surface $L(\alpha,\beta)$ for quenched NB20, generated from the Weibull^{++}7^{TM} software, is shown below.

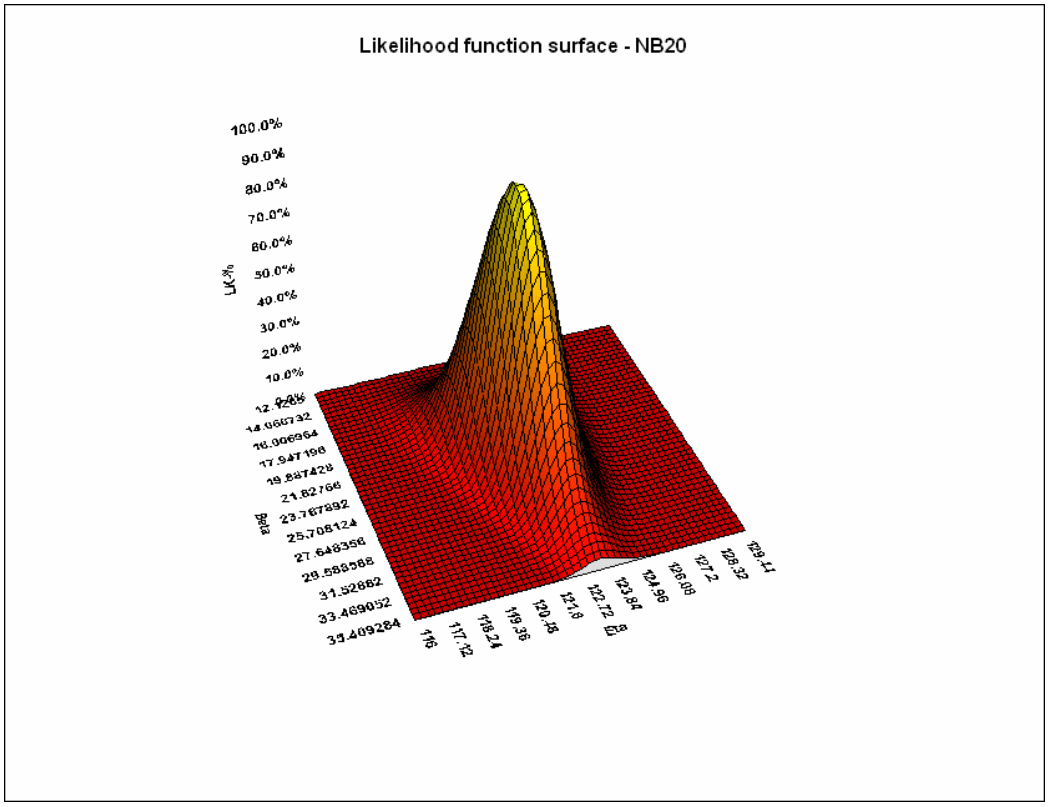

Figure 6.4: Likelihood function surface for quenched NB20. (The axis labelled "eta" corresponds to α.) Contours drawn parallel to the α,β plane would indicate the Likelihood Ratio (see below) confidence limits of these parameters.

However, MLE parameter estimation is also known to be biased, especially for β, with the effect becoming worse for small n and the bias in α becoming worse for small β. Cacciari *et al.* [6.17] have reviewed the various unbiasing techniques available, which can be split into two categories. Firstly, there are those methods that modify the estimator equations (7.6) and (7.7) above in some way, such as the Jacquelin [6.18] technique. By contrast, the Ross [6.19] and Harter-Moore [6.20] methods operate on the parameters which have already been obtained by conventional MLE. The methods are more or

less reliable for given sample sizes, parameter values and whether or not the data sets are censored or not. Cacciari *et al.* [6.17] for example, demonstrate by Monte Carlo analysis that the Bain-Engelhart estimated data is *worse* for $\beta>1$ and small sample sizes than unestimated data.

Once the estimated parameters have been obtained, it is necessary to estimate their confidence intervals. These can be determined from the ratios of the likelihood values of the estimated data to those of associated with other values of α and β. If likelihood ratios are not available, confidence bounds can be obtained from Monte Carlo datasets. Monte Carlo data tables have even been published using pivotal quantities (statistics which are a function only of the sample size) [6.17].

6.3 Statistical background: optimal parameter estimation

The manual for the Weibull $^{++}7^{TM}$ software does not give any indication that an unbiasing technique is used in its MLE procedure. Moreover, it advises that for sample sizes of less than 30, the rank regression technique should be used. This is clearly at odds with received wisdom [6.1] and it was therefore necessary to use a Monte Carlo procedure to determine the best-behaved method. It is important to note that the following discussion does not concern the general applicability of the MLE and RRX methods for Weibull analysis. Rather, the suitability of these methods is discussed for the particular range of parameters pertinent to this study, using this particular piece of software. A constant nominal value of α was chosen to be 100, with β and n ranging from 0.5 to 25 and 5 to 25 respectively. This more than covers the extremes of n and β found experimentally. For example, sections 6.4 and 6.5 of this chapter contain inferences made on datasets with $n>14$. For each pair of (n,β) values, 1000 datasets were generated and analysed using MLE and rank regression with respect to the x (RRX) and $\ln(\ln(F(x))$ (RRY) values, producing sets of estimated α and β parameters, $<\alpha>_i$ and $<\beta>_i$, where $0<i<1001$.

Figures 6.5-6.7 below illustrate typical differences seen using the three estimators on 1000 datasets for $\beta=6$ and $n=20$. The median and mean estimated parameter lines are consistently biased away from the true

parameter line for the MLE and RRY methods. We conclude that for these for this sample size and shape parameter, RRX gives the best estimation of the population line.

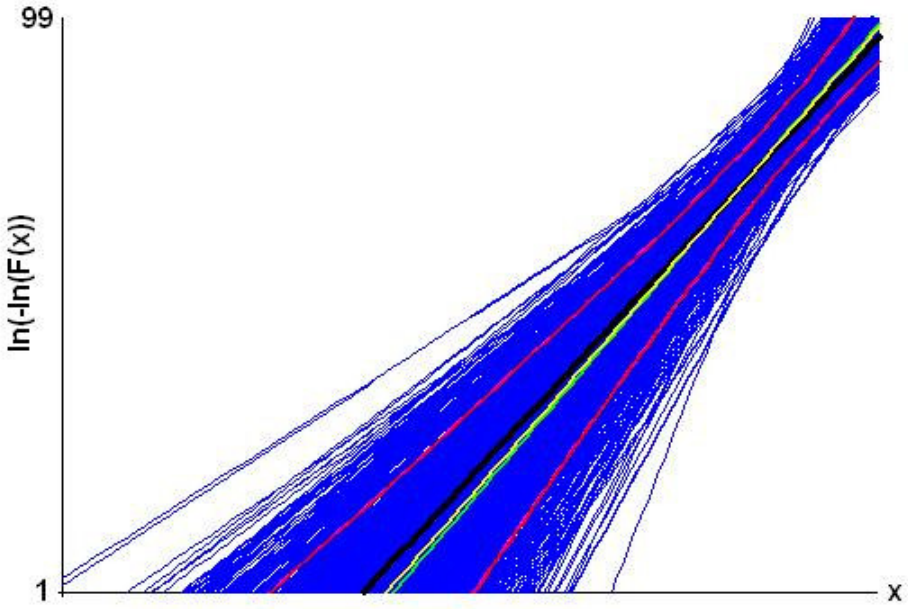

Figure 6.5: MLE estimation on 1000 Monte Carlo datasets with *n*=20 and *ß*=6, 90% 2-sided confidence intervals. Black line = original parameter line, green and yellow lines correspond to mean and median <*α*> and <*ß*> parameters respectively. A systematic anticlockwise deviation is seen in the estimated data lines with respect to the original parameter line; this corresponds to an overestimation of *ß*.

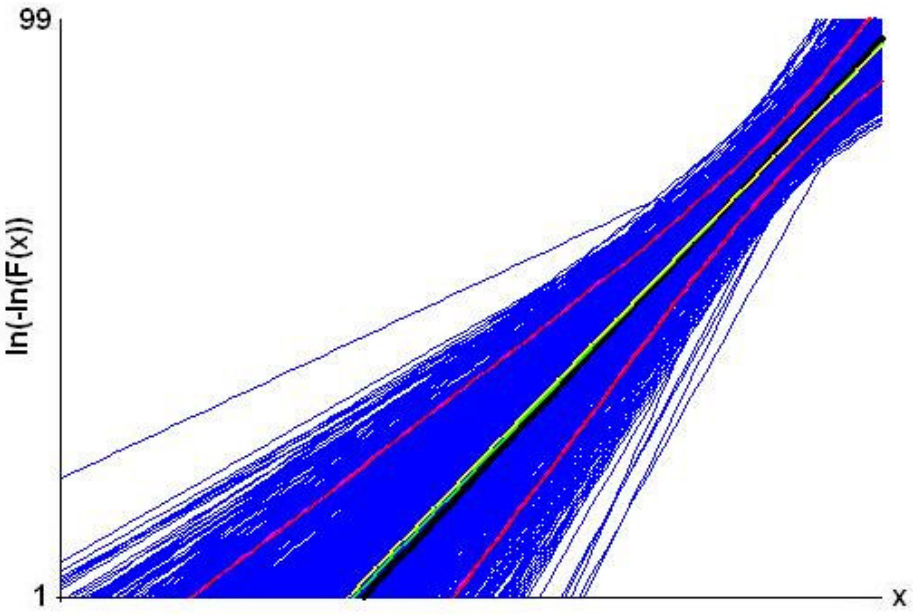

Figure 6.6: As Figure 6.5 but with RRY estimation and a clockwise bias in the data lines corresponding to the estimated parameters.

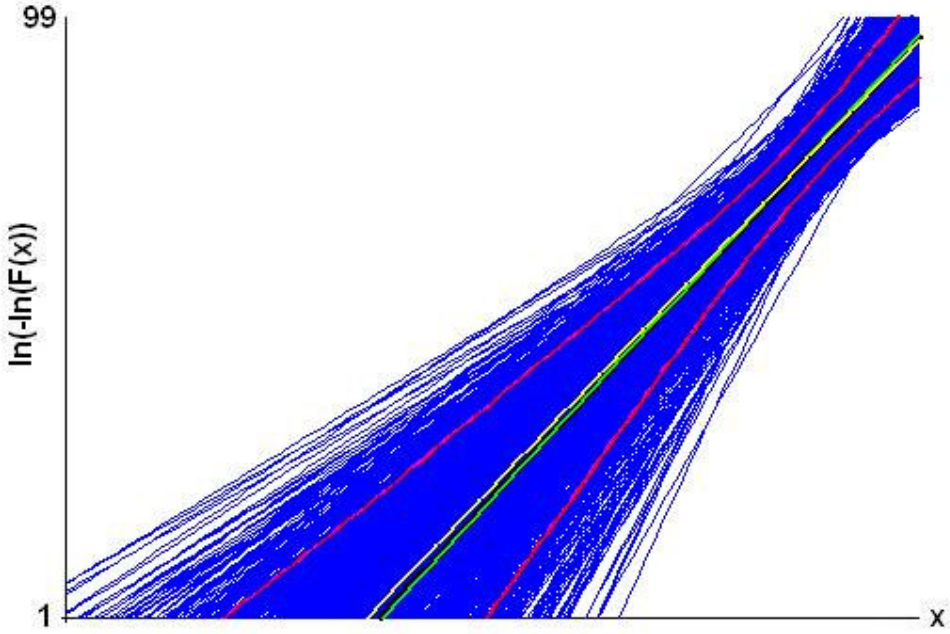

Figure 6.7: As Figures 6.5 and 6.6 above but with RRX estimation. RRX in this case is a better estimator than both RRY and MLE.

Figures 6.8-6.11 illustrate the behaviour of the RRX- and MLE-calculated <*α*> and <*ß*> as a function of both *n* and *ß*. Confidence bounds for <*α*> and <*ß*> are given as a half-width:

$$\textit{95\% uncertainty parameter} = \frac{1.96\sigma}{\sqrt{1000}} \qquad (7.8)$$

where *σ* is the standard deviation in <*α*> or <*ß*>. In each of these figures, the upper and lower plots show the bias and uncertainty in the estimated parameters respectively. Common to all the graphs is that the bias and uncertainty in <*α*> and <*ß*> decrease with increasing *n*. Apart from this, however, the RRX and MLE estimators show very different behaviour.

Figure 6.8 shows that even for large sample sizes, the MLE algorithm employed by Weibull^{++}7^{TM} will consistently overestimate. At *n*=25, for example, the bias in <*ß*> is at least 1.06 – 1.1% = +1.05. With *n*=15, it could be as high as 1.12 +1.6% = +1.14. In contrast the RRX-calculated <*ß*> shown in Figure 6.9 is much more stable. Here, the bias has a 95% confidence upper *maximum* of +1.05 at *n*=20. It is interesting, though, that whereas a clear correlation between *ß* and the bias in <*ß*> can be seen in the MLE-estimated data, the corresponding RRX-estimated bias is highly random with respect to *ß*. Also of interest is that the confidence parameters for <*α*> in Figures 6.10 and 6.11 are massively dependent on the true value of *ß*, unlike the <*ß*> above. The dependence on sample size is weak by comparison. For sample sizes above 15, both the MLE and RRX techniques can be trusted to estimate *α* to within 1%, provided the *ß* > 2. Fortunately, this requirement is met by all of the data obtained experimentally. Both MLE and RRX are therefore used below.

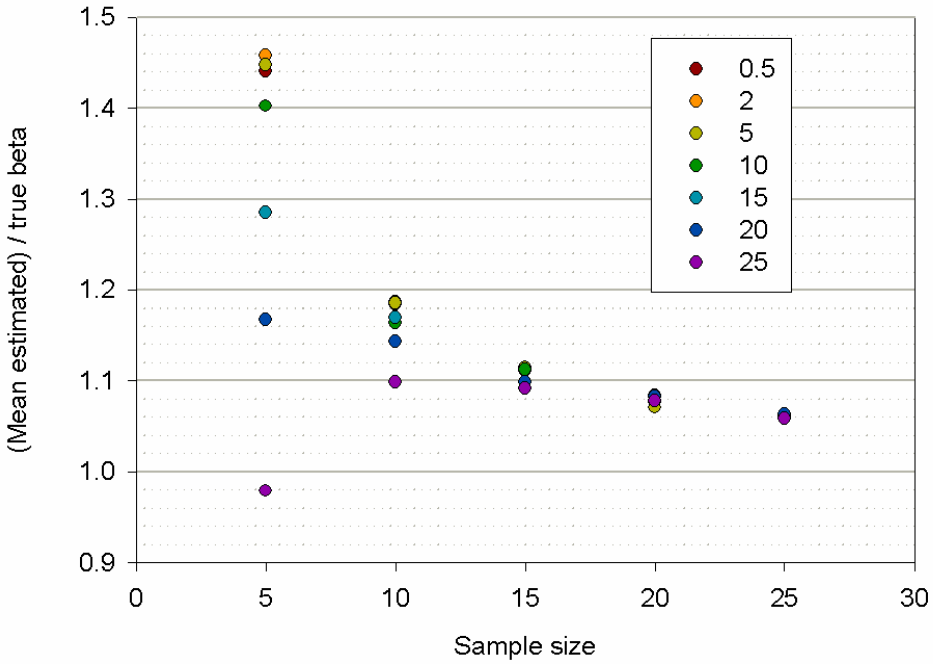

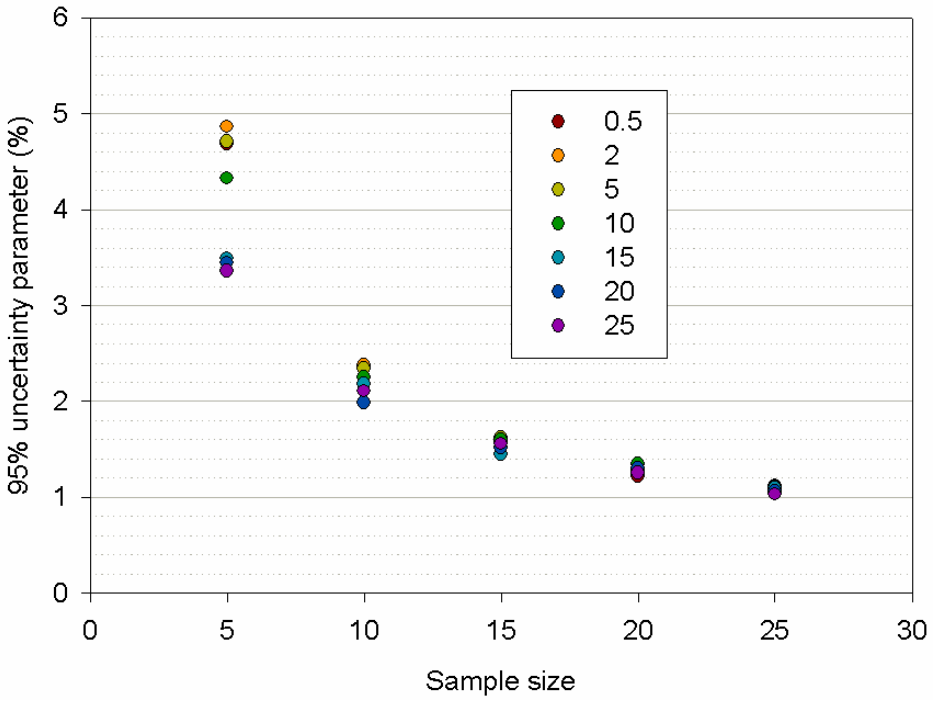

Figure 6.8: Predicted bias in MLE-estimated <*ß*> from Monte Carlo data. The technique is seen consistently to overestimate *ß* for all *n*. Key: *ß*.

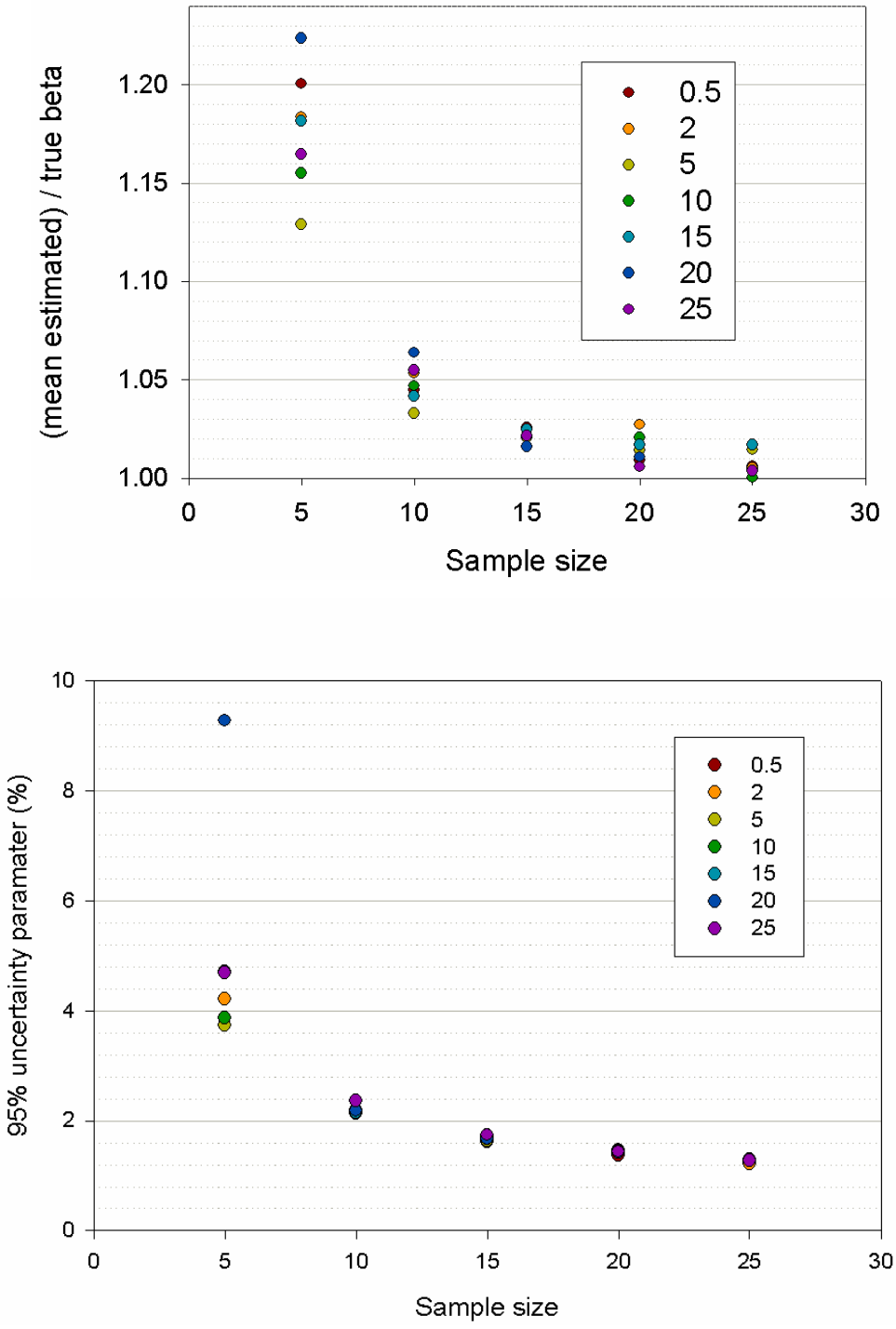

Figure 6.9: Predicted bias in RRX-calculated *ß* from Monte Carlo data. The RRX procedure is demonstrated to be much more reliable than MLE for these data. Key: true *ß*.

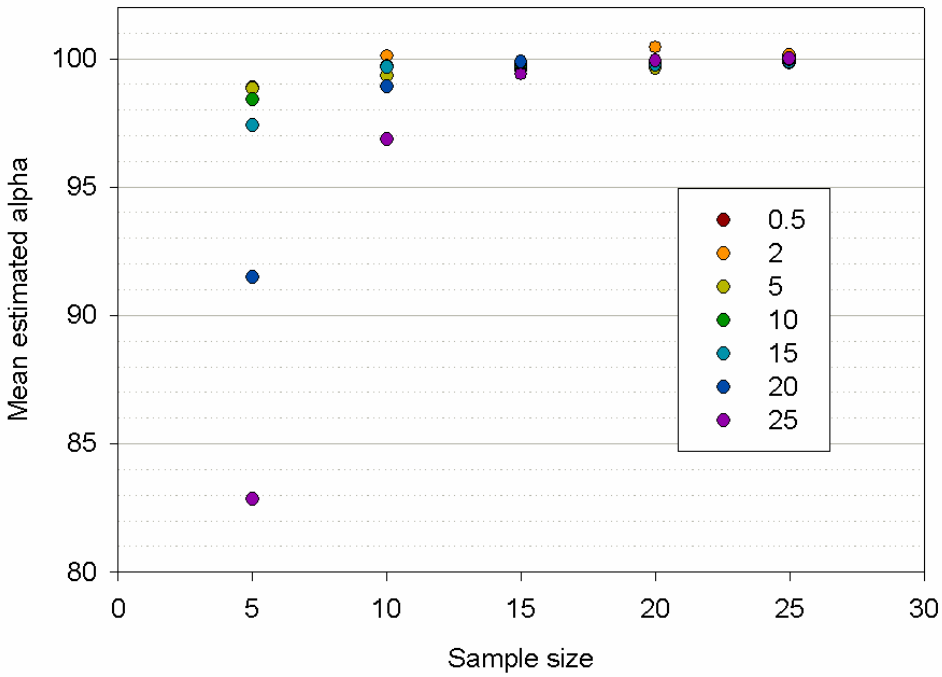

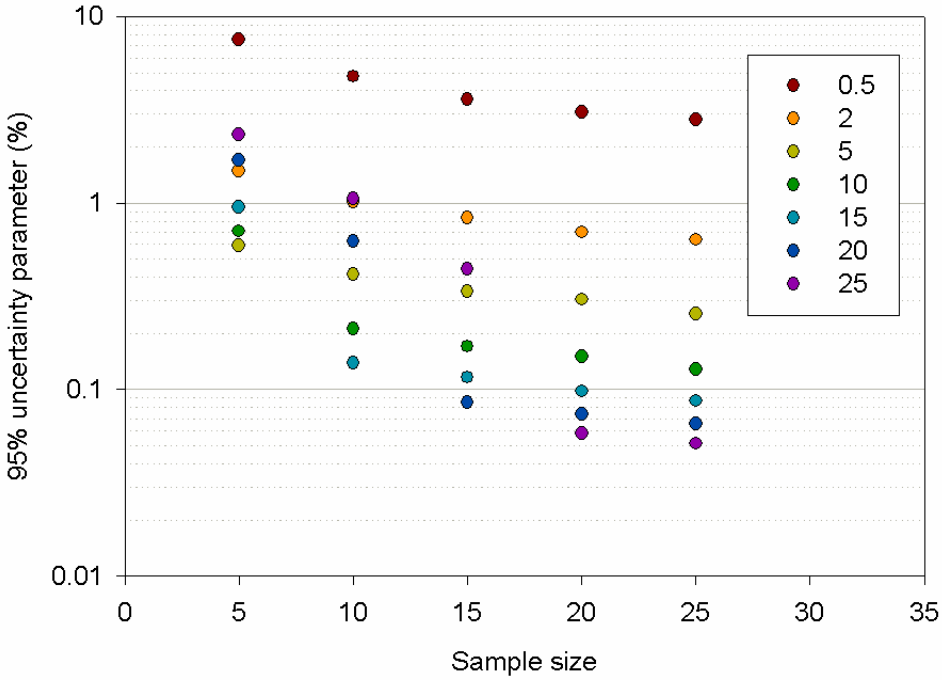

Figure 6.10: Predicted bias in MLE-calculated *<α>* from Monte Carlo data. MLE can be trusted provided *ß*>2 and *n*≥15. Key: true *ß*.

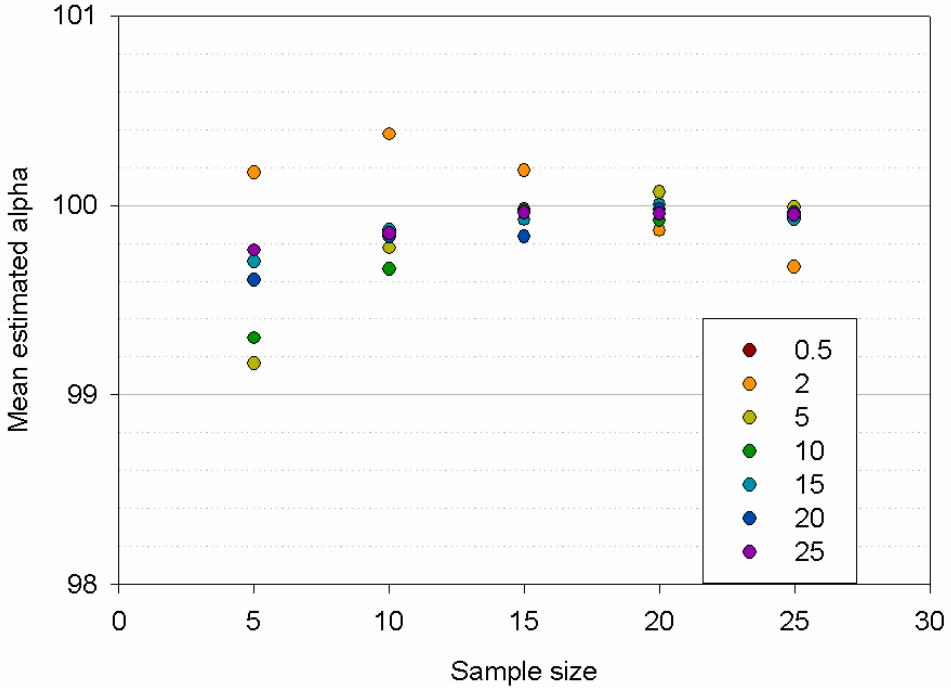

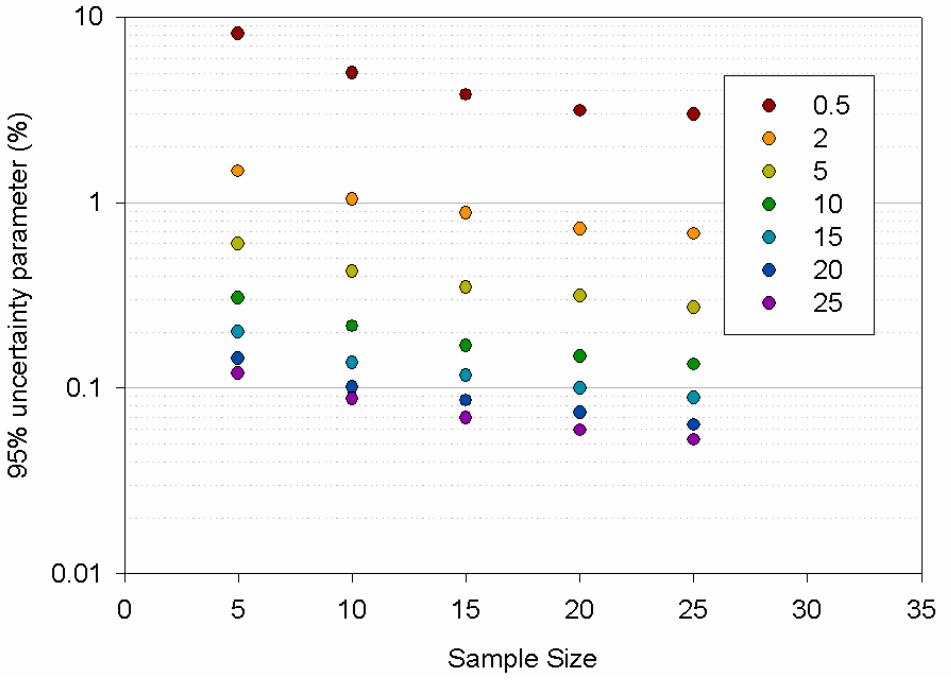

Figure 6.11: Predicted bias in RRX-calculated *<α>* from Monte Carlo data. Again, RRX out-performs MLE. Key: true *ß*.

6.4 Non-parametric estimation

It is also possible to determine confidence bounds for ranked experimental data without the assumption of a parametric model. Increased generality is thereby obtained at the expense of wider confidence bounds. As the data in this report are not interval or right-censored (at worst, the only points removed from the data are taken from the bottom end, with a corresponding reduction in sample size) the ideal way of doing this would be to generate beta binomial confidence bounds. Returning to equation (6.3) and setting the left hand side to 0.5 yields the median rank estimator. If instead the left hand side is first set to 0.05 and then 0.95, a 90% confidence interval in cumulative probability will have been generated.

Unfortunately, the Weibull$^{++}7^{TM}$ software does not support this technique for raw data. Instead, the Kaplan-Meier technique for interval-censored data is employed (in our case with ability to censor is redundant.) The following equation is used to estimate the cumulative failure probability:

$$F_i(x) = 1 - \prod_{j=1}^{i}\left(\frac{a-b}{a}\right), i = 1,.....,n \qquad (6.8)$$

where a is the number of units available to fail in the jth interval (ie that have not already failed or been suspended) and b is the number of units failing in this interval. In this work, b=1 and equation (6.8) reduces to the crude:

$$F_i(x) = \frac{i}{n}, i = 1,.....,n-1 \qquad (6.9)$$

The software then generates confidence bounds via the Greenwood formula [6.21] to estimate the variance in $F_i(x)$:

$$\sigma^2_{F_i(x)} = \sum_{j=1}^{i}\frac{(F(x))^2\left(\frac{b}{a}\right)}{a\left(1-\frac{b}{a}\right)}, i = 1,.....,n \qquad (6.10)$$

6.5 Methodology: summary

Although the ball-bearing breakdown method suffers from the distinct disadvantage of partial discharge and surface tracking phenomena, it is by far the most efficient method of generating large enough sets of data on which to perform robust statistical analysis in small amounts of time. Further efficiency can be realised by coupling time and applied field into a single ramped parameter, though this does mean that the ability to discern specific types of stochastic processes in the time domain is lost. Nonetheless, the objective of this work is not to probe the underlying physical mechanisms, but simply to study the breakdown statistics as a function of masterbatch type and loading level. It is a satisfying result that chi-squared testing favours the use of a 2-parameter Weibull distribution for this analysis.

Monte Carlo analysis has been used to decide whether MLE or RRX is the more reliable parameter estimator. For the range of beta parameters and sample sizes used in this work, RRX has overwhelmingly been shown to be favourable. Nonetheless, there is value in using both techniques in the discussion below, for the sake of comparison. As there is no physical basis for using the Weibull distribution for these samples, there is no physical basis for trusting Weibull confidence bounds on the empirical cdfs. Therefore, a simple but powerful non-parametric technique by the name of Kaplan-Meier estimation is also used below in order to bolster confidence in the conclusions that are drawn.

6.6 Results

Breakdown data were obtained from samples for both masterbatches as a function of loading level. Data for α and β are summarised in Table 6.2. A nomenclature is used in which the isothermal crystallisation temperature in °C is given in brackets, “q” indicating that the sample was quenched. The colours in the table indicate subsections of the data under which the samples were randomised and atmospheric conditions were roughly constant. To each

Material	MLE		RRX	
	α – kV mm^{-1}	ß	α– kV mm^{-1}	ß
NB0=NC0(q)	146.6	6.2	146.6	5.9
NB5(q)	162.7	8.0	163.7	5.9
NB10(q)	166.9	12.4	167.4	10.0
NB20(q)	175.1	17.2	175.0	23.9
PERef1	158.3	24.3	159.3	21.3
PERef2	151.7	22.3	151.4	25.3
NC5(q)	152.3	8.4	152.4	7.5
NC10(q)	144.1	6.0	144.6	5.1
NC20(q)	155.4	22.8	155.7	18.9
PERef3	163.6	14.2	163.0	16.4
NB0=NC0(q)	149.7	9.4	151.0	6.9
NB0=NC0(117)	148.1	8.0	148.0	7.1
NB5(q)	164.6	18.6	164.4	20.6
NB5(117)	165.3	25.3	165.0	26.7
NB20(q)	172.4	17.8	171.7	22.1
NB20(117)	170.9	19.0	170.6	20.4
NC20(q)	150.4	12.1	151.3	9.3
NC20(117)	156.4	11.0	157.3	8.4

Table 6.2: Estimated Weibull parameters from RRX and MLE for all data in Figures 6.16-6.19. Each colour block groups samples that were tested together over 4 days, shuffled to eliminate experimental drift.

subsection belongs a reference sample PERef1, PERef2 and PERef3, pressed from LDPE. It is apparent from these data that a monotonic increase in breakdown strength and reduction in scatter result from increasing the amount of Nanoblend masterbatch. Corresponding to the yellow section of the table, Figure 6.12 compares the Weibull plots for the Nanoblend-based systems to an LDPE reference. The striking feature of these data is that sample NB0=NC0(q) has a markedly lower breakdown strength than the LDPE reference sample. This effect can be attributed to ageing during extrusion. A distribution of residence times results in an aged morphology as shown in Figure 2.13, which may affect the high voltage conduction characteristics of the material due to the introduction of a new trap distribution. (The low field behaviour proved to be unaffected by ageing, as discussed in the previous chapter.)

The other significant conclusion to be drawn from Figure 6.12 is that NB0=NC0(q), NB10(q) and NB20(q) are significantly different from each other at the 90% confidence level. NB10(q) is not significantly different from the reference blend, illustrating the usefulness of this filling level for mitigating the effects of extrusion ageing. The Weibull plot for NB5(q) is particularly interesting as it appears to contain two clusters of data corresponding to the NB0=NC0(q) and NB10(q) populations respectively. This would argue for competing mechanisms which are both operating at sufficiently small loading levels. If much larger quantities of data were available, it would be an informative exercise to correlate these sub-populations to morphological features. The value in a non-parametric approach as a statistically robust tool for confirming these conclusions is shown by Figure 6.13. We can be quite sure of the validity of the confidence bounds, as they do not rely on any assumed distribution.

Whereas the breakdown data for the Nanoblend systems are promising, the same cannot be said of the Nanocor systems, as shown in Figure 6.13, lower plot. At best, it can be argued that there is a slight improvement in breakdown strength for NC20(q); smaller loadings, however, only serve to increase the scatter below E_b relative to the LDPE reference. Although NC5(q) and NC20(q) exhibit better performance than NB0=NC0(q), the NC10(q) does not. This contrasts to the monotonic relationships both between breakdown

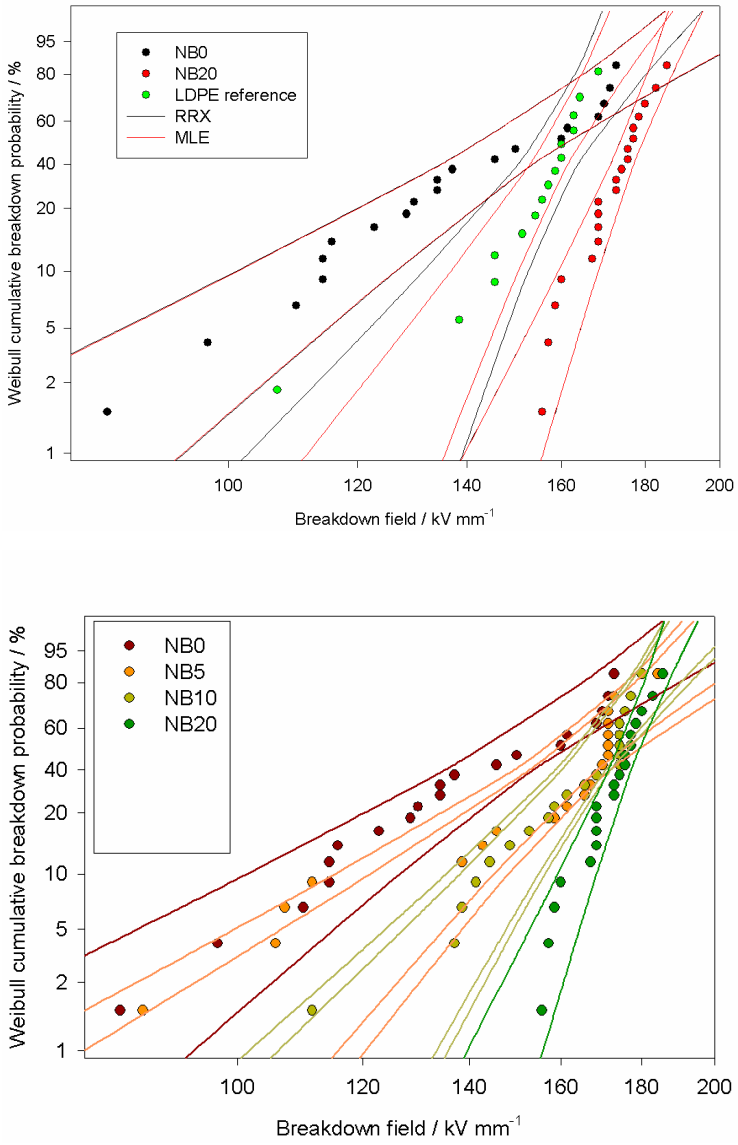

Figure 6.12: Influence of Nanoblend loading level on breakdown statistics relative to a non-extruded LDPE reference sample. NB20 serves to more than nullify the detrimental effect of extrusion. Outer confidence bounds: RRX. Inner confidence bounds: MLE. All materials quenched.

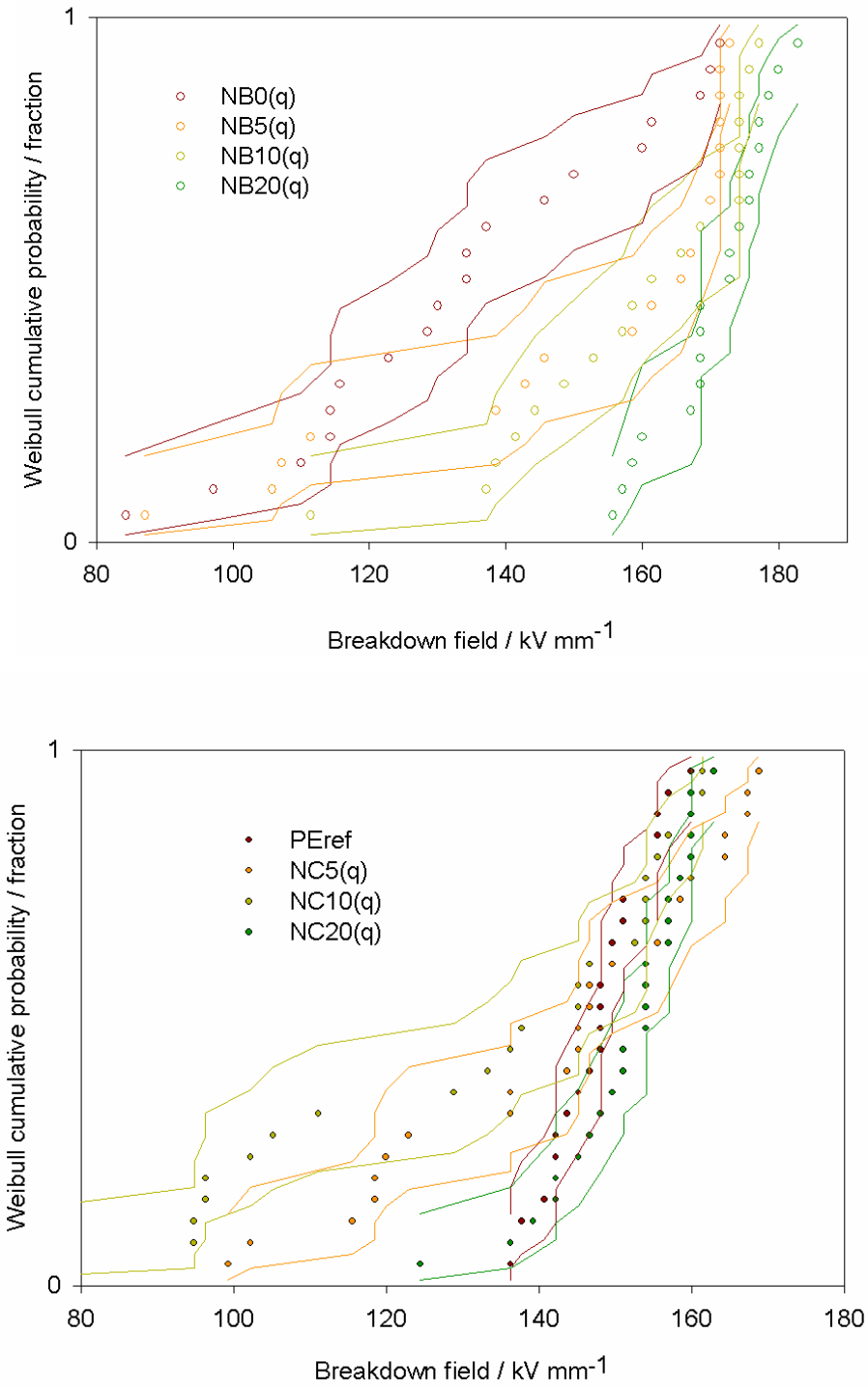

Figure 6.13: Kaplan-Meier plots with 90% confidence bounds for Nanoblend and Nanocor systems. Both systems improve breakdown strength and shape relative to NB0=NC0, although the Nanoblend masterbatch does so more effectively.

strength / shape parameter and loading level seen in the Nanoblend-based systems.

It was a cause of concern that the LDPE reference sample used for the quenched Nanocor systems had a breakdown strength nearly 7 kV mm^{-1} lower than that used to characterise the Nanoblend systems. These correspond to PERef1 and PERef2 in Table 6.2 respectively. It was decided, therefore, to compare all of these data to equivalent quenched sets obtained during subsequent isothermal crystallisation / quenching experiments. Reassuringly, as can be seen in Table 6.2, the breakdown strength of PERef3 (used for this final set of experiments) is much closer to PERef1, confirming the anomalous nature of PERef2. In the corresponding Weibull plot, Figure 6.14, the lower *ß* exhibited by PERef3 is due to three anomalously high values; PERef1 and PERef3 are not otherwise significantly different.

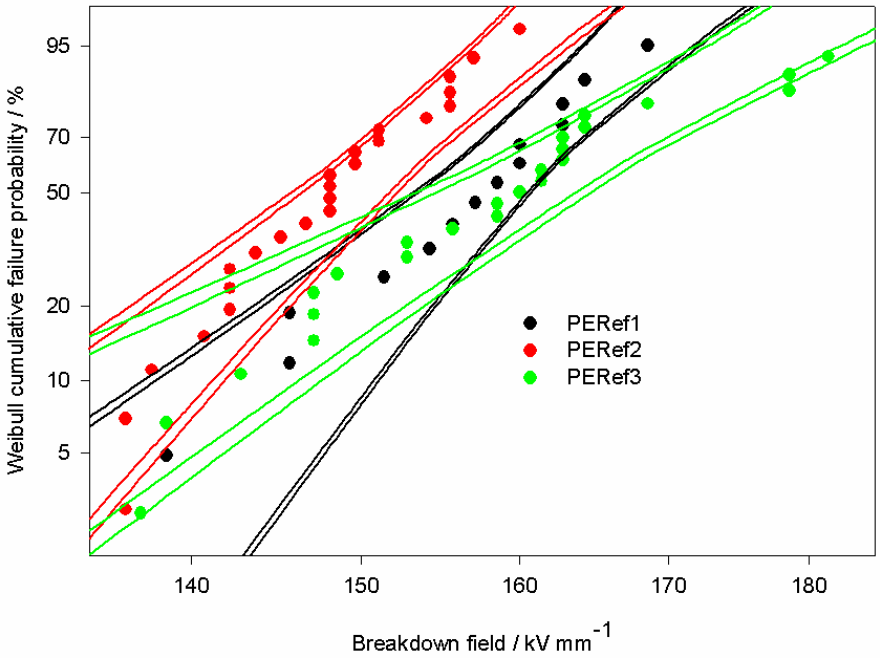

Figure 6.14: Comparison of the LDPE reference samples used in this study. PERef1 has a significantly lower breakdown strength than the other samples. Outer confidence bounds: RRX. Inner confidence bounds: MLE.

Comparison of the data for NB0=NC0(q) and NB20(q) shows that this does not affect our conclusion that the Nanoblend-based materials have higher breakdown strengths than the unfilled polyethylene blend.

It is important to establish that there are good reasons why PERef2 should exhibit significantly different breakdown statistics to PERef1 and PERef3. One possible candidate explanation is the ambient temperature. PERef2 was studied during the summer, with an ambient laboratory temperature of 23-25 °C, whereas PERef1 and PERef3 were analysed during the winter, with an ambient temperature of 15-17 °C. Oakes [6.5] studied the effect of temperature (77-350 K) on the AC ramp breakdown statistics of 100-700 µm recessed polyethylene films with graphite electrodes. Pentatene / toluene and transformer oil were used as the immersion media from -100 °C - +25 °C and from 25 °C to 40 °C respectively. Between 0 °C and 40 °C, E_b drops from ~650 kV mm^{-1} to ~600 kV mm^{-1}. Although the response does not appear to be linear (Oakes tentatively suggests a critical Fröhlich temperature around 30 °C,) this would correspond to a change in the region of 1 kV mm^{-1} °C^{-1}, which would be entirely consistent with the variation in our results. Guerin *et al.*[6.22], studied the DC breakdown strengths of 100 µm LDPE film between Rogowski-profiled electrodes. Although they did not measure below room temperature, a drop of 30 kV mm^{-1} was found between 25 °C and 45 °C, which by extrapolation below room temperature would nonetheless corroborate our hypothesis.

In our samples, however, we must also consider the effect of partial discharging in micro-pockets of silicone oil between the electrodes and the sample. Yehia *et al.*[6.23] studied the DC breakdown strengths of oxygenated and degassed silicone oil (50 cS) between a nickel-plated steel sewing needle and a 5 mm-diameter earthed steel sphere. The experiments were all conducted at room temperature. For a negative needle, and for a needle-sphere spacing of 50 µm, the oxygenated oil had a ~50 % higher breakdown strength than the degassed oil. For a positive needle, the increase was smaller, at ~20 %. One cannot reject the possibility that, even if we concede that the variation of oxygen content will only be a very weak function of temperature [6.28], the actual discharging process may itself be temperature dependent. Although a degree of variability can be seen between the three sets of data, the

possibility of variation *within* each of these need not be feared. This is because rather than testing all 5 disks of each material at the same time, the materials were alternated such that any variation in external factors would appear only to increase the overall scatter in the data.

Note also that the *ß*-value according to MLE is 18.6 for the second NB5(q) sample in Table 6.2 (green region), compared to a previous 8.0 for the first (yellow region.) The RRX-estimated value has increased from 5.9 to 20.6. This is simply a consequence of increasing the sample size from 20 to 25. Of all the systems associated with PERef3, there was no reason to censor any of the low values, whereas 4 points were removed from both NB5 samples in the green section of Table 6.2 that could legitimately be assigned to the NB0=NC0(q) or NB0=NC0(117) datasets. Due to the smaller sample size, progressive censoring of NB5(q) would have removed too many points due to the apparent change in mechanism at high fields.

Figure 6.15 shows the effect of isothermal crystallisation on these samples. Based on the work of Hosier [6.4] it was expected, at least in NB0=NC0, that isothermal crystallisation would significantly increase the breakdown strength. On the contrary, if there are any effects present they are very subtle and would require much larger sets of data for their validation. Even the higher ß seen in NB5(117) is an artifact of censoring a 211 kV mm^{-1} breakdown event. It is curious that the only other anomalously high event can be seen uncensored in the corresponding NB5(q) population, Figure 6.19. A Kaplan-Meier plot was used for the NC20 samples due to the second population of points which appear below 140 kV mm^{-1} (most likely another consequence of differences in temperature and humidity.) When these points are removed, the remaining populations are still not significantly distinct at the 90 % level.

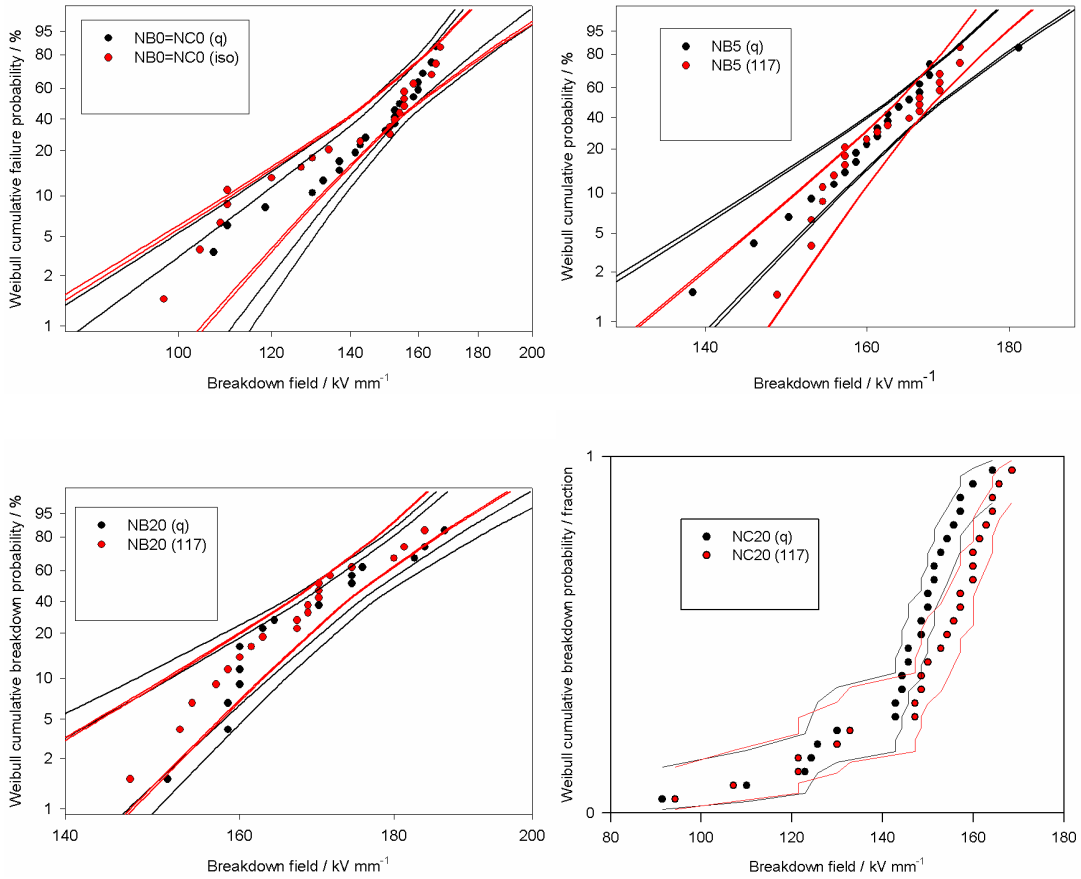

Figure 6.15: Effect of crystallising samples at 117 °C on breakdown strength. Isothermal crystallisation does not significantly increase the breakdown strengths of these materials. Outer confidence bounds: RRX. Inner confidence bounds: MLE.

We attribute the unexpected behaviour of NB0=NC0 to extruder degradation. Another run of NB0=NC0 and NC10 was processed using a much finer feedstock. These materials are designated 2/NB0=NC0 and 2/NC10 respectively. It is estimated that they were processed with residence times approximately one half of NB0=NC0 and NC10. Although it was very difficult to decide by optical microscopy whether they contained less degradation, 2/NB0=NC0 was visibly whiter than NB0=NC0. The effect of isothermal crystallisation on the breakdown behaviour of 2/NB0=NC0 is shown in Figure 6.16. The breakdown strength in the isothermally crystallised sample is

significantly increased, as originally expected. However, the corresponding data for 2/NC10 shown in Figure 6.17 indicate that the addition of o-MMT nonetheless suppresses the effect. However, the breakdown strength of 2/NC10(q) is substantially greater than NC10(q) and marginally greater than 2/NB0=NC0. It is ~50 kV mm^{-1} greater than that of a poorly dispersed reference (produced, as before, by solution in xylene) containing 90 : 10 : 10 w/w/w BPE : LPE : I30P. It is not clear whether this improvement is due to reduced degradation or a result of shorter residence times leading to a different particle size distribution.

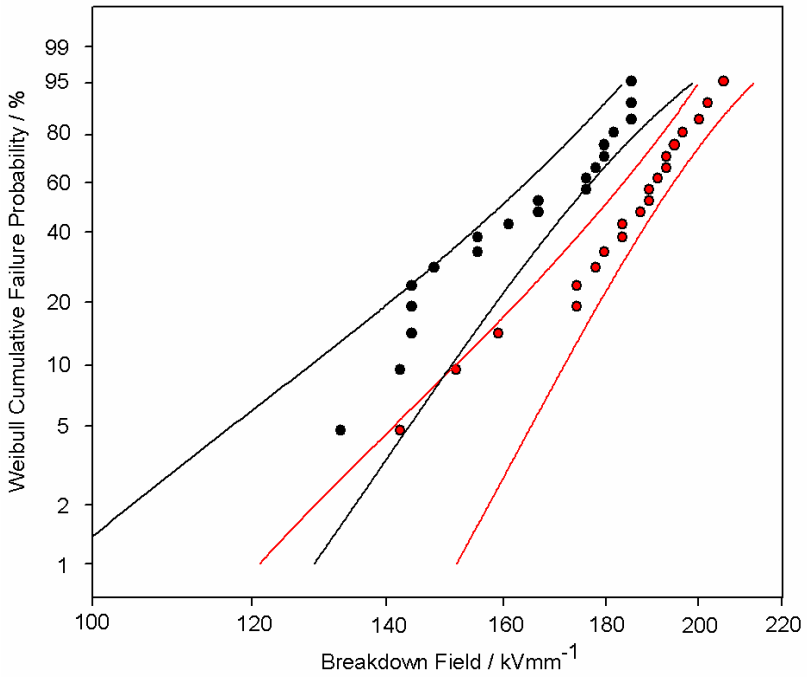

Figure 6.16: Weibull plots for material 2/NC0=NB0 with differing thermal histories. Red: Isothermal crystallisation at 117 ℃. Black: Quench. Isothermal crystallisation significantly increases the breakdown strength. Confidence bounds: MLE

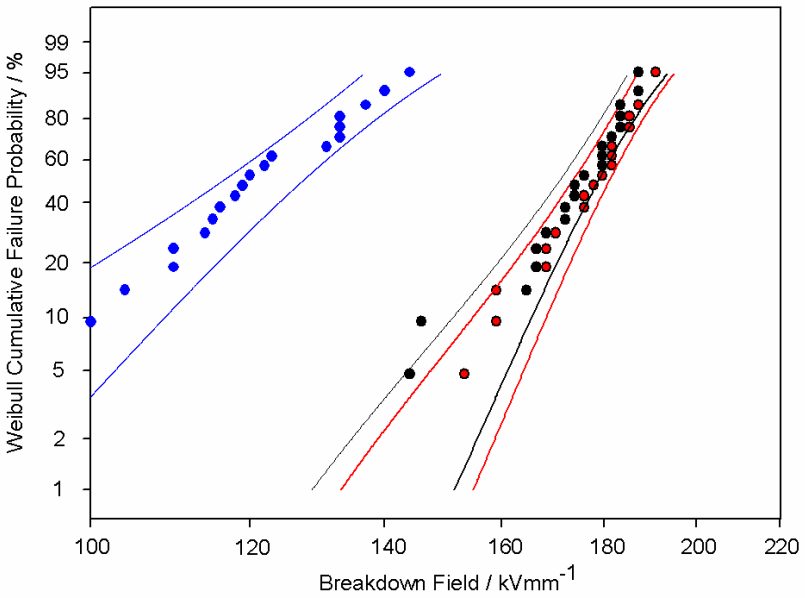

Figure 6.17: Weibull plots for 2/NC10. Red and black indicate same thermal histories as in Figure 6.16. Blue: poorly dispersed reference with same %wt o-MMT content as 2/NC10. Breakdown strength of 2/NC10 than poorly dispersed reference, but not increased by isothermal crystallisation. Confidence bounds: MLE

6.7 Discussion

The loss of isothermal strengthening seen in Figure 6.17 for material 2/NC10 may be a combination of reduced spherulite size or the result of a new distribution of electrical scattering, mechanical toughening or surface discharge resistance centres. The distinct population of low breakdown strengths seen in the NC20 plot of Figure 6.15 suggests that the larger filler particles may be acting as defect initiators [6.25-6.26]; such behaviour is typified by the behaviour of the poorly dispersed reference blend. The defects can be morphological, as mismatched thermal expansion coefficients between the particle and the matrix can combine with chemical incompatibility to result in voiding at the interface. They can also distort the electric field through charge trapping, or via permittivity or conductivity mismatch under AC and DC conditions respectively. Breakdown strength-reducing processes may compete

with enhancement processes to produce the non-monotonic loading level – breakdown strength behaviour seen in the Nanocor-based systems.

The encouraging results for the Nanoblend systems are supplemented by data from NB0(MA) and NB10(MA) shown in Figure 6.18. In this case, it is clear that in NB10(MA) the cumulative probability of failure drops off rapidly below 180 kV mm^{-1}. This is a useful result for a design engineer when optimising the maximum working stress of a system.

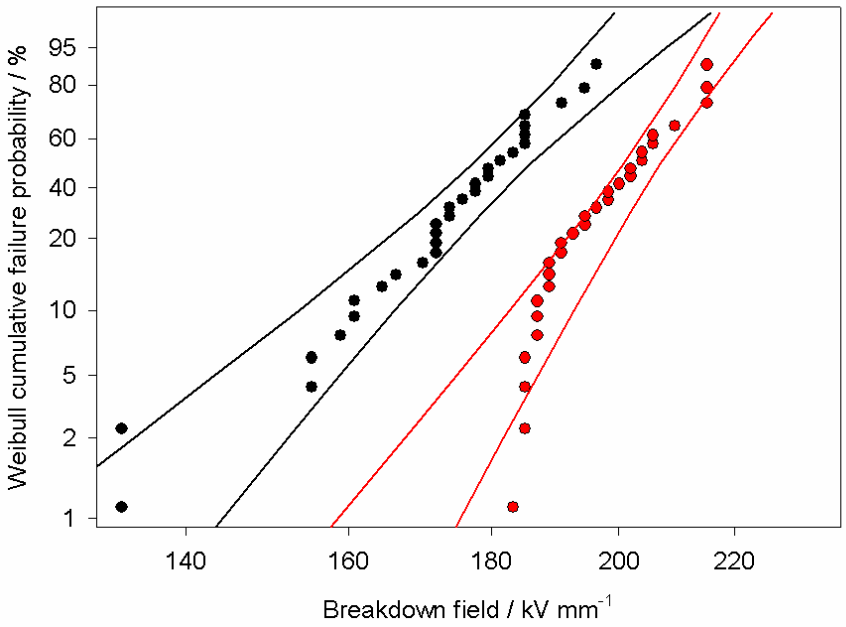

Figure 6.18: Weibull probability plots for material NB10(MA) (right) and NB0(MA) (left) following quenching. It is seen that the breakdown strength of the filled sample is increased by ~11%, and that a threshold voltage appears to be introduced. Confidence bounds associated with MLE estimation.

There is much evidence in the literature of the potential for breakdown strength enhancement in nanocomposite systems. Provided that the nanofillers are adequately dispersed, the electrical breakdown strength of the resulting system is higher than its unfilled counterpart. For example, breakdown by electrical treeing was studied in an epoxy composite filled with a mixture of

micro- and nano-silica [6.27] and improved endurance times were observed compared with a simple microcomposite. This feature was related to the denser, more tightly-packed tree structures that evolved in the presence of the nanofiller. This is a graphic illustration of the kind of scattering processes discussed above. Roy *et al.*[6.28] suggest that the increased DC breakdown strength of an XLPE / silica nanocomposite is linked with a reduced charge carrier mobility through a free volume breakdown mechanism with enhanced scattering. More tentative conclusions have been made in connecting breakdown statistics with space charge behaviour. A recent paper [6.29] has discussed the improved DC breakdown strengths of magnesium oxide/LDPE nanocomposites in terms of the suppression of packet charge. However, another paper reports that internal fields due to space charge build up in nano-alumina / LLDPE materials regularly initiated sample breakdown during pulsed electroacoustic testing [6.30].

In Chapter 2, the various types of breakdown mechanism in polymers were discussed. It was noted that it there is still a lack of consensus even in simple polymers (eg. polyethylene) concerning whether the intrinsic breakdown mechanism is of an electronic or thermo-mechanical nature. Since the breakdown process will ultimately involve electrical and thermo-mechanical activity, the real difficulty is in deciding which precedes the other. A thorough knowledge of macroscopic parameters such as Young's modulus (and its temperature variation,) thermal conductivity, electrical conductivity and space charge profile are of use only in distinguishing between macroscopically-predictive models. (Space charge has been shown to build up in XLPE cables even under 50Hz applied stress [6.31].) If more advanced microstructural models are required to explain the data, including local inhomogeneities in electric field distribution and space charge density, the task of selecting the best model becomes even more difficult. Our situation is even more indeterminate than this, however, because of the electrode-surface discharge processes which result in heating, erosion and modified charge injection behaviour. We can be quite confident about the improved behaviour of the Nanoblend-systems under these experimental conditions, but we cannot be sure why.

The effect of isothermal crystallisation on the dielectric strength of polyethylene blends is another case in point. The explanation given for this [6.4] is that isothermal crystallisation leads to space-filling spherulites which present the breakdown process with a more tortuous path. This could describe one of five processes:

●A more tortuous path to frustrate the progress of electrical treeing. This does not apply in the thin-film situation.

●More resistance to a filamentary thermal breakdown event.

●More resistance to filamentary electromechanical failure.

●More scattering of hot electrons, limiting their energies. A consequence of lamellar material having a negative electron affinity.

●More surface resistance to partial discharge erosion. As the amorphous material is preferentially eroded from the surface, emerging spherulites offer increasing defence to further erosion.

In any case, it seems that if the material spends too long in the extruder barrel, this strengthening mechanism is no longer able to overcome the intrinsically weakened amorphous material.

It is possible to simulate the effect of surface erosion due to electrical activity by means of laser ablation [6.32]. A Synrad CO_2 class 4 laser source was used. The melt-pressed sample, measuring 7 * 7 * 2 mm^3, was placed in an aluminium chamber with an interlock before applying a power of 12 W. This was low enough for the beam not to burn through the sample, but it was also considered that any time dependence in ablated volume at this power level is a function of changing material parameters alone rather than thermal conduction out of the sample [6.32]. Estimation of hole depths by optical microscopy was not able to detect any significant differences between NB0=NC0, NB5 and NC5 at 60 J, at around 1.0 mm. However, the hole depths of NB20 and NC20 remained constant at ~0.4 mm over a range of applied energies from 20 J to

60 J, showing that the highly-loaded materials are highly resistant to degradation in this energy range. Nonetheless, the mechanism responsible for this is apparent even in the lightly-loaded materials, as judged by SEM.

Figure 6.19 was generated by exposing an ablated sample of NB5 to the standard permanganic reagent of Chapter 4, comprising 1% w/v $KMnO_4$: (1:2:5 v/v/v H_2O: H_2PO_4: H_2SO_4). There seem to be two clay-rich phases present that could contribute to the erosion resistance. Firstly, an ashy region is present which is essentially separate from the bulk material. It might be expected that this layer is friable and consequentially useless for designed ablation-resistant materials, though it did manage to survive a 2-hour acid etching process under vigorous mechanical agitation. Secondly, a clay-rich melt zone exists inside the surface of the pit. This will contribute to degradation resistance in at least one of four ways:

● Enhanced mechanical stiffness acting to reinforce the ablation pit by spreading local stresses.

● Enhanced heat capacity, diffusing heat energy away from hot spots. Direct evidence for this is seen in the banded crystallisation in the lower image of Figure 6.19. From Chapter 3, these objects will have been formed slowly over the space of several minutes as the filler cooled. Hosier [6.32] observed micron-sized (alumina and zinc oxide) fillers to glow red hot in laser ablation experiments at similar powers.

● Enhanced thermal conductivity – the thermal conductivity of clay is over twice that of polyethylene [6.33]. This will act to diffuse the heat away from the ablation zone. If the heat transport takes place primarily by percolation through the network of clay particles, it is approprate to think of this as a barrier effect. Otherwise, it would be more appropriate to think of the clay of modifying the intrinsic thermal conductivity of the matrix.

● Furthermore, the possibility that there may be a significant optical barrier effect should not be neglected. A significant drawback in comparing laser ablation with electrical erosion is that the clay may provide a barrier effect in

terms of photon reflection and scattering. This question could be investigated through the use of in-situ CCD detection of reflected light, together with simple light-scattering experiments. For the time being, inferences made concerning enhanced electrical erosion resistances based on laser ablation data must remain working hypotheses rather than foregone conclusions.

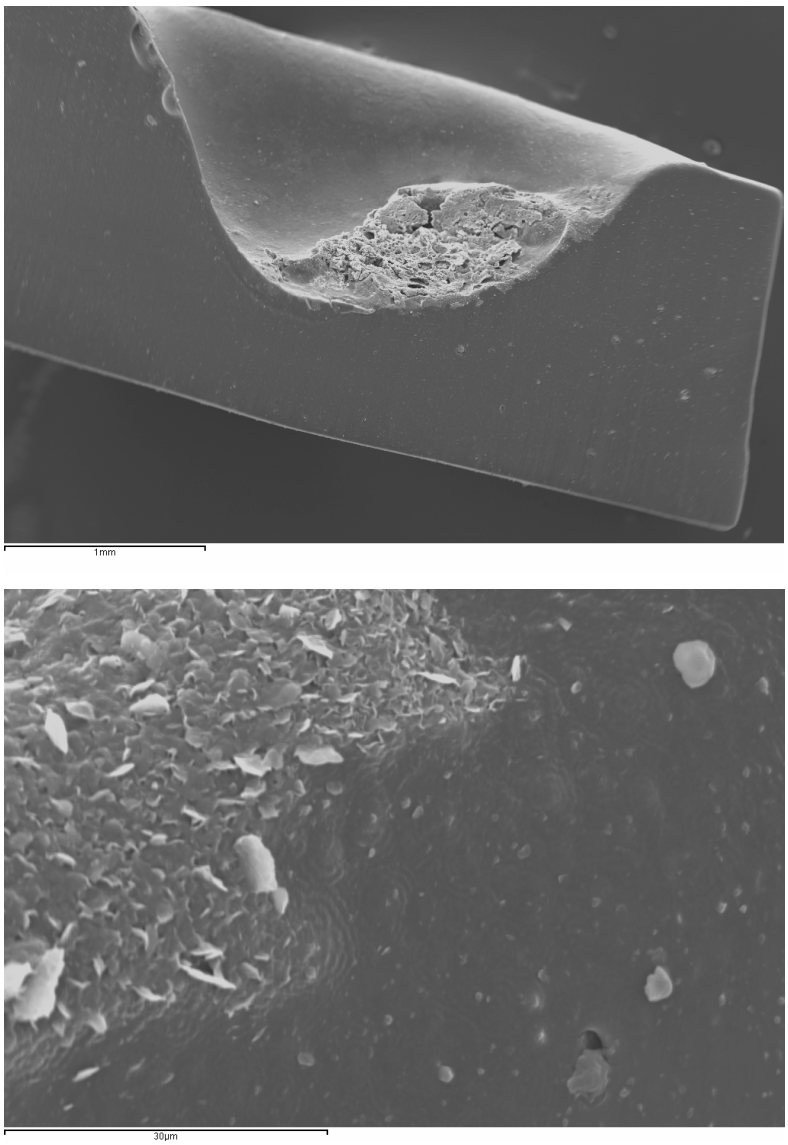

Figure 6.19: SEM images of ablated hole in material NB5. Upper image: formation of incipient protective inorganic layer. Lower image: Zoomed-in image of arrowed region in upper image. A clay-rich melt zone has formed with a high heat capacity, as judged by the presence of banded spherulitic growth.

6.8 Conclusion

AC ramp breakdown statistics have been obtained for the Nanoblend- and Nanocor-filled materials at various loading levels. Ball-bearing electrodes were used to generate a sufficiently large amount of breakdown data to be analysed under a Weibull distribution. Both MLE and RRX were used to generate confidence bounds, providing additional graphical information about the goodness of fit to a Weibull distribution. It was found that the Nanoblend-filled systems have consistently higher breakdown strengths than the unfilled polyethylene blends. The increase in breakdown strength varies monotonically with loading level, though the data are decidedly non-Weibull at low to intermediate loading levels. Rather, there are at least two master populations associated with unfilled and highly-filled samples which, under sufficiently small loading levels, can be seen together. A non-parametric approach was therefore used to establish the significance of the differences between the datasets.

It was found that the Nanocor masterbatch also had the potential to improve the breakdown strength and shape parameter, albeit in a much less robust way than the Nanoblend masterbatch. It is believed that breakdown events are very sensitive to the larger clay agglomerates found in the Nanocor-based materials, and that this sensitivity can be exacerbated through a synergism with degradation products originating from the extruder.

This experiment is not suitable for making inferences about the electrical strengthening mechanisms present in these materials; despite half a century of work, this remains a controversial topic even in simple materials. However, laser ablation data suggest that the filled materials may offer greater resistance to electrical erosion. Whether they also have a higher breakdown strength in terms of solely bulk processes remains to be seen. However, even the bulk processes governing practical engineering systems, namely partial discharge and electrical breakdown, are extrinsic in the sense that they are involved with the formation of new surfaces. It is highly probable, therefore, that the Nanoblend-based systems would offer superior performance in these respects too.